Experimental investigation on the grain-scale compression behavior of loose wet granular material

Vinh Du Than, Patrick Aimedieu, Jean-Michel Pereira, Jean-Noël Roux, Anh Minh A.M. Tang

Experimental investigation on the grain-scale compression behavior of loose wet granular material

Vinh-Du Than[1,2], Patrick Aimedieu[1], Jean-Michel Pereira[1], Jean-Noël Roux[1], Anh Minh Tang[1]

[1] Université Paris-Est, Laboratoire Navier, UMR 8205, École des Ponts ParisTech, IFSTTAR, CNRS, 77455 Marne-la-Vallée Cedex 2, France

[2] The University of Danang, University of Technology and Education, Department of Civil Engineering, Danang, Vietnam

Corresponding author:

Dr. Anh Minh TANG

Ecole des Ponts ParisTech

6-8 avenue Blaise Pascal

77455 MARNE-LA-VALLEE

France

Tel: +33.1.64.15.35.63

Email: anhminh.tang@enpc.fr

Abstract

The behavior of model granular materials (glass beads) wetted by a small quantity of liquid forming capillary bridges is studied by one-dimensional compression test combined with X-ray computed tomography (XRCT) observation. Special attention is paid to obtain very loose initial states (initial void ratio of about 2.30) stabilized by capillary cohesion. XRCT-based analyses involve spherical particle detection adapted to relatively low-resolution images, which enable heterogeneities to be visualized and microstructural information to be collected. This study on an ideal material provides an insight into the macroscopic compression behavior of wet granular materials based on the microstructural change, such as pore distance distribution, coordination number of contacts, coordination number of neighbors, number of contacts per grain.

Keywords: Wet granular material; Microstructure; One-dimensional compression; X-ray computed tomography; Grain-scale analysis

List of notation

a	size of standard volume
b	size of extended volume
$\langle d \rangle$	average diameter
$d_{\min}$	minimum diameter
$d_{\max}$	maximum diameter
e_0	initial void ratio
e	void ratio
EV	extended volume
$f(r)$	signature curve
Φ_0	initial solid fraction
$g(r)$	radial distribution function
i, j, k	voxel indices
i_C, j_C, k_C	center position of detected sphere
$\mathbf{I}(i, j, k)$	intensity at voxel (i, j, k)
$\nabla\mathbf{I}(i, j, k)$	gradient vector at voxel (i, j, k)
N	number of particles
N_C	number of pairs in contacts
$p(r)$	average number density of particles
$q(i, j, k)$	vector from (i_C, j_C, k_C) to voxel (i, j, k)
r	radii of particles / radial distance
SV	standard volume
Si	step of scan (S1, S2, S3, S4)
z	total coordination number

$z(h)$ coordination number of close neighbors

1 Introduction

Granular materials appear in various natural and industrial processes. They are often composed of individual grains that vary in shape, size and surface texture. Such parameters can remarkably affect the packing of granulates and their contact distribution characteristics. In the case of wet granular materials, the existence of liquid menisci between particles plays a key role in the overall behavior of the assembly. Capillary cohesion bestows to these materials specific mechanical features that do not exist with dry grains, such as the ability to form stable structures with very low densities, and a strong sensitivity to external applied forces. So far, there are a lot of experimental studies on their macro- and micro-mechanical behaviors, such as: cohesive soils [1, 2], wet beads [3, 4], loess [5, 6], wet sand [7–9], among others. These works evidenced the link between the macroscopic mechanical behavior and the microstructure change. However, few works have yet focused on the grain-scale behavior.

Currently, the mechanical grain-scale behavior of a wet granular material is usually investigated by discrete element methods using 2D and/or 3D simulations [10–24]. These studies precisely characterized the change of microstructure such as coordination numbers (of contacts, of distant interactions, of compressive and tensile contacts), radial distribution function, force chains, distribution of forces between particles, *etc*. under the applied external forces. However, few works have compared numerical simulations (*e.g.* using the discrete element method) and experimental results in order to validate the numerical method [25–30].

X-ray computed tomography (XRCT) has tremendous potential due to its ability to carry out volumetric imaging inside the specimen. It has become a widely used technique and is appropriate for numerous types of materials including particulate and porous materials [31,

32]. Furthermore, this technique has been used in several studies to investigate the microstructure of granular materials under mechanical loading [8, 33–39]. Most of these works focus on the analysis of granular packing in dense states and with large-size particulates. Few works have experimentally investigated the mechanical grain-scale behavior of wet granular materials by using XRCT [40–44].

In this paper, we present an experimental investigation, by means of XRCT, on a loose wet granular material. A cylindrical sample constituted of thousands of glass beads with liquid bonds were subjected to an oedometric compression test, which consisted of several compression steps. At each step, a XRCT scan was performed. The sample heterogeneity is first analyzed in order to get a general understanding of the pore-scale compression behavior. The main objective of the present works is to give a further insight into the grain-scale compression behavior of loose wet granular materials.

2 Experiments

2.1 Material and specimen preparation

The investigated material consists of industrial spherical glass beads (diameter equals 87 µm to 110 µm with an average value of 100 µm). The specific density of this material is equal to 2,460 $kg.m^{-3}$. A Scanning Electronic Microscopic image of a glass bead is shown in Figure 1. The image shows that the surface of the bead is slightly damaged (beside the presence of some tiny dust grains) which makes it not perfectly smooth.

To prepare the specimen, the glass beads were first mixed with water to reach gravimetric water content (mass of water divided by mass of solid) of 3.5 %, which ensured that the specimens always remained in the pendular regime. The wetted glass beads were then placed

on a 200 µm opening sieve installed 80 mm above an oedometric cell. Afterward, a machine vibrated the sieve vertically in order to gradually pass the wet glass beads through the sieve and let them fall into the cell.

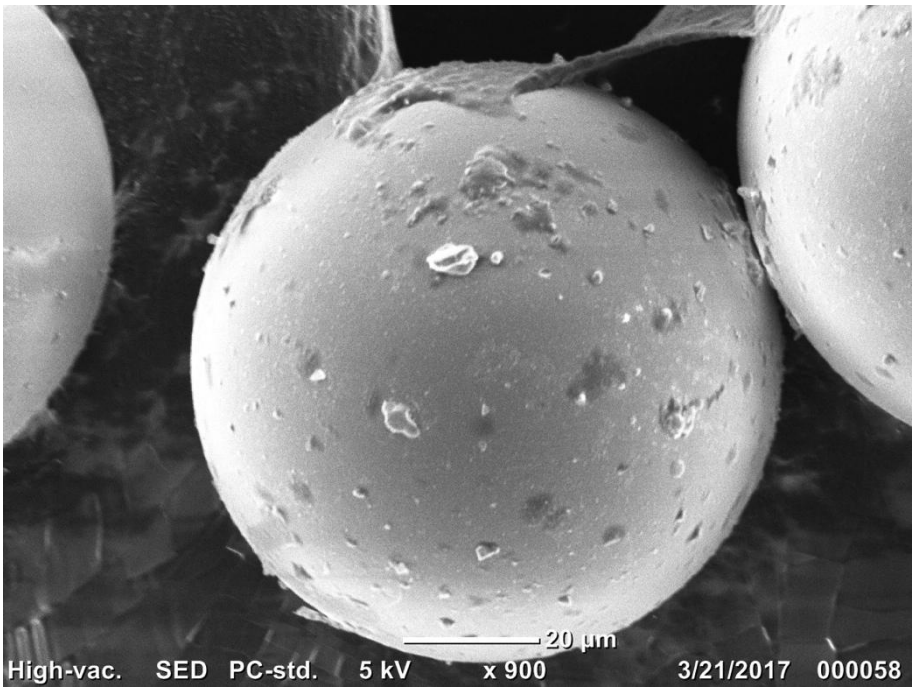

Figure 1: Scanning Electronic Microscopic image of a glass bead.

This procedure allowed the preparation of loose specimen with a porosity n = 0.70 (corresponding to a void ratio e_0 = 2.33, a solid fraction Φ_0 = 0.30, and a degree of saturation of S_r = 3.7%). This degree of saturation, smaller than 5 %, corresponds to the pendular regime following Newitt & Conway-Jones [45].

2.2 Oedometric compression behavior

In order to perform oedometric compression tests, the specimen (50 mm in diameter and 20 mm in height), prepared by the procedure described above, was carefully placed on a loading platform. A piston was fixed to a load cell to measure the vertical load applied to the sample.

A LVDT sensor measured the displacement corresponding to the compression. The cell was then moved upward with a rate of 0.5 mm/min.

Figure 2 illustrates the compression curves of two specimens (CT01 and CT02). Based on the shape of these curves and the range of vertical stress, three stages could be identified. Firstly, under low stresses (σ_v < 0.1 kPa), void ratio *e* is slightly decreased. Secondly, the void ratio is sharply decreased. Finally, under higher stresses (σ_v > 10 kPa), the void ratio is gradually decreased.

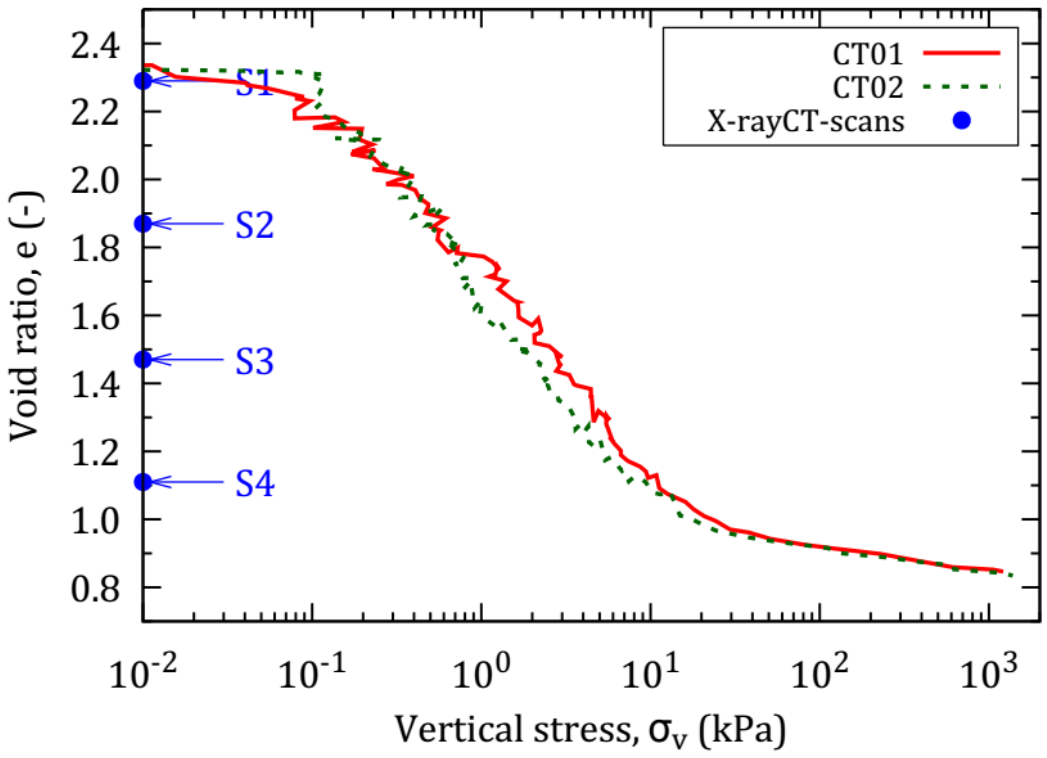

Figure 2: Void ratio versus vertical stress during oedometric compression tests for two specimens. The circle points show the conditions of XRCT scans.

2.3 X-ray computed tomography

In the present work, XRCT scans were performed by using an UltraTom microtomography device. Prior to the observations with XRCT, the specimen (20 mm in diameter and 10 mm in height), prepared by the procedure described in the section 2.1, was compressed to reduce its void ratio to e = 2.29 (position S1, see Figure 2). Once this state was reached, a XRCT scan (global scan) was performed for the whole specimen. The central zone of the sample (10 mm in diameter and 80% of the sample's height) was subsequently scanned (local scan). Figure 3 shows an example of reconstructed 3D images obtained from these scans. The voxel size was 13 µm for the global scan and 6.5 µm for the local scan. Following the scan corresponding to the position S1, the same scanning procedure was repeated three times to obtain the XRCT images corresponding to positions S2, S3 and S4, as shown in Figure 2. One piston having appropriate length was designed for each position. That allowed the correct control of the height of the sample to be scanned (there was no pressure applied to the piston during the scan). A global scan took 80 min and a local scan took four hours. During these scans, the piston was maintained above the sample to avoid evaporation of water. The small gap between the piston and the cell (0.05 mm) allows draining air during compression while avoiding evaporation during the scan. The cell and the pistons were made of Polymethyl methacrylate (PMMA) in order to optimize the quality of the XRCT images.

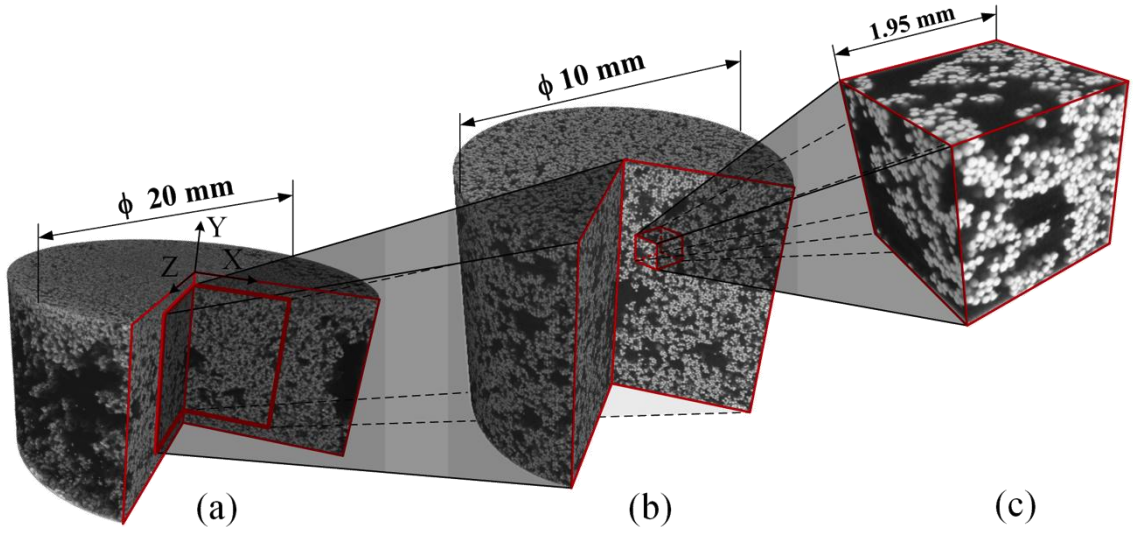

Figure 3: (a) Global scan, (b) local scan, and (c) investigated cube.

2.4 Analysis of sample heterogeneity

The reconstructed 3D samples, obtained by global scans at four compaction levels, are shown in Figure 4. It is well recognized that the density is not homogeneous within the cylindrical sample, especially at the periphery where more voids can be observed; higher densities and fewer voids exist at the top and the bottom of the sample. There are also several large voids in the center of the specimen in the initial stages (Figure 4*ab*). Similar results were observed previously on unsaturated loose volcanic sands [44]. This heterogeneity is due to the specimen preparation, and also to the boundary conditions imposed by the oedometer cell. In other words, during the specimen preparation, the friction between the cell and the grains limits the movement of grains. At higher compaction levels (Figure 4*cd*), the structure is strongly rearranged in the central layers because the loosest state was observed in this region (horizontal band) while the structure is slightly affected in the bottom and top layers.

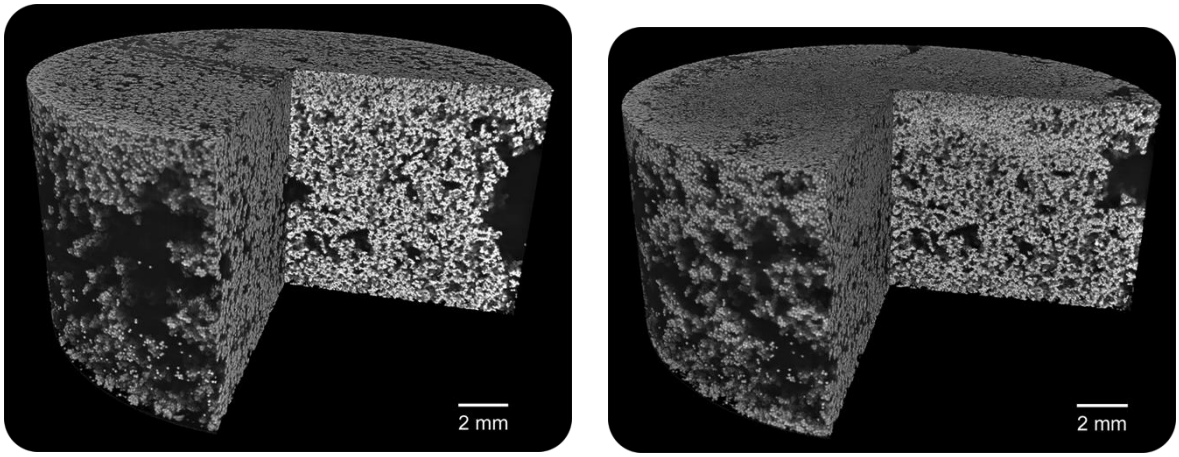

(a) (b)

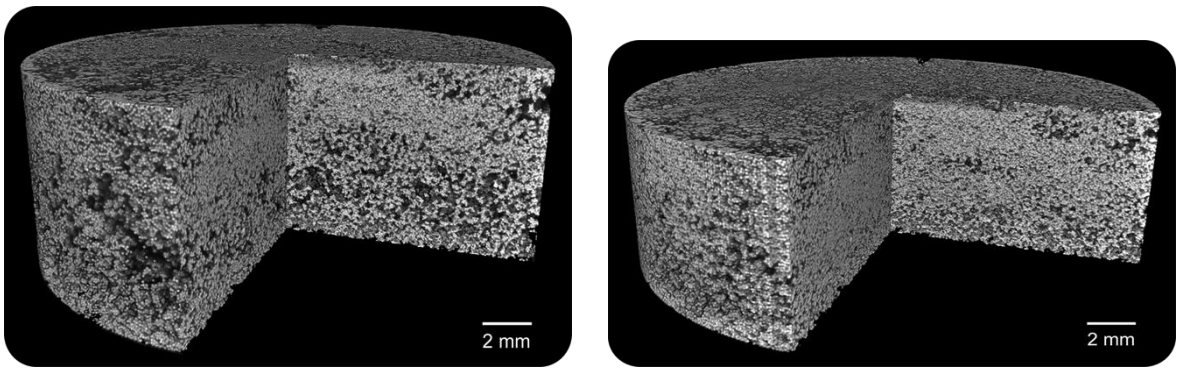

(c) (d)

Figure 4: 3D reconstructed images of the sample at different compaction levels. (a) S1, (b) S2, (c) S3, and (d) S4.

The grey level histograms are shown in Figure 5. Depending on the compaction level, two peaks are more or less visible on each histogram. The first one on the left-hand side corresponds to air-dominated voxels. Its number is smaller at a denser state. The peak on the right-hand side corresponds to grain-dominated voxels and its number did not change during compaction.

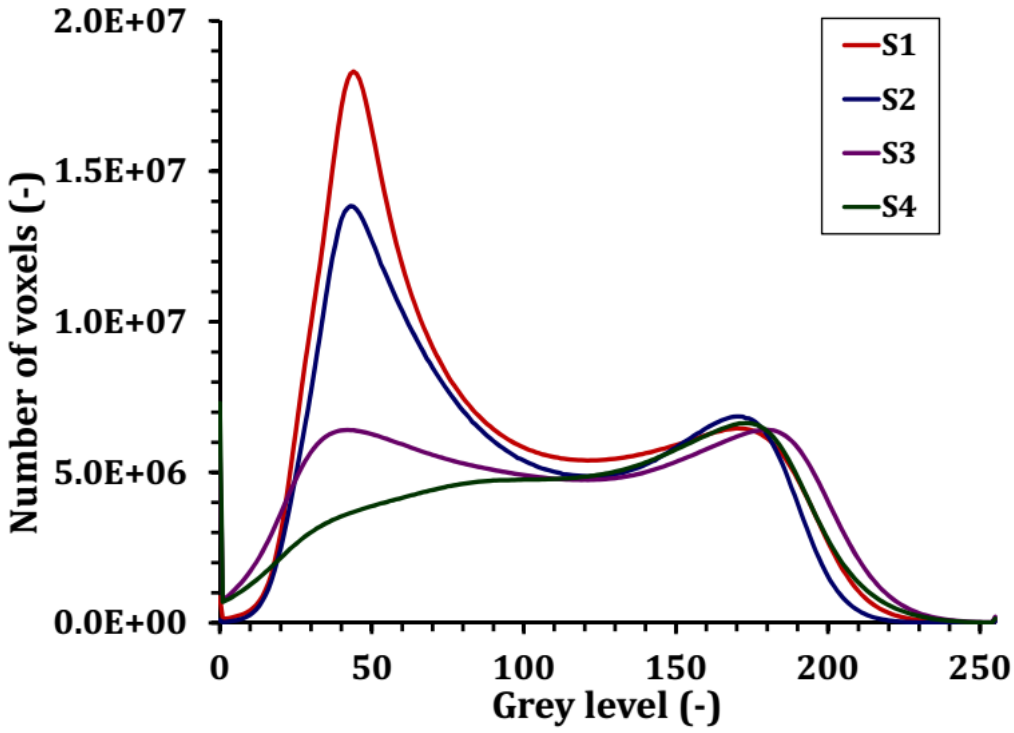

211 Figure 5. Grey level histogram for the four scans.

212

213 The void ratio distribution according to the elevation (*h*) during the compression is illustrated
214 in Figure 6. The void ratio is directly calculated from the tomography images. To obtain void
215 ratio values, a grey-level threshold value was chosen for each scan, based on their grey level
216 histogram. This value (around 130) was determined within the interval between the peaks
217 corresponding to the air phase and the aggregates, respectively. The IsoData method [46] was
218 chosen for the segmentation process. After thresholding, the aggregates (white) and the air-
219 filled voids (black) are clearly distinguished. The void ratio is then recalculated by dividing
220 the number of black voxels by the number of white voxels of the segmented image. Note that
221 for the four global scans, the void ratios obtained by this method are similar to the imposed
222 values; the average void ratios of the four curves (2.31, 1.91, 1.48 and 1.14, corresponding to
223 S1, S2, S3 and S4) are very close to the macroscopic ones, which are 2.29, 1.87, 1.47, and
224 1.11 respectively. In this study, as the volume of water is smaller than 5% of volume of voids
225 at the beginning, the presence of water has been ignored during the whole image analysis
226 process. The binarization and watershed approach are not used because of the low resolution
227 of the images. The voxel size was 13 μm, for the global scan, that means each grain has
228 around 7 pixels diameter. In other words, the contact boundary of grains is not clear to
229 separate. In fact, we had tried to apply the sub-voxel algorithm in order to increase the
230 resolution of image, especially at the contact boundary but this method increases significantly
231 the computation time.

232

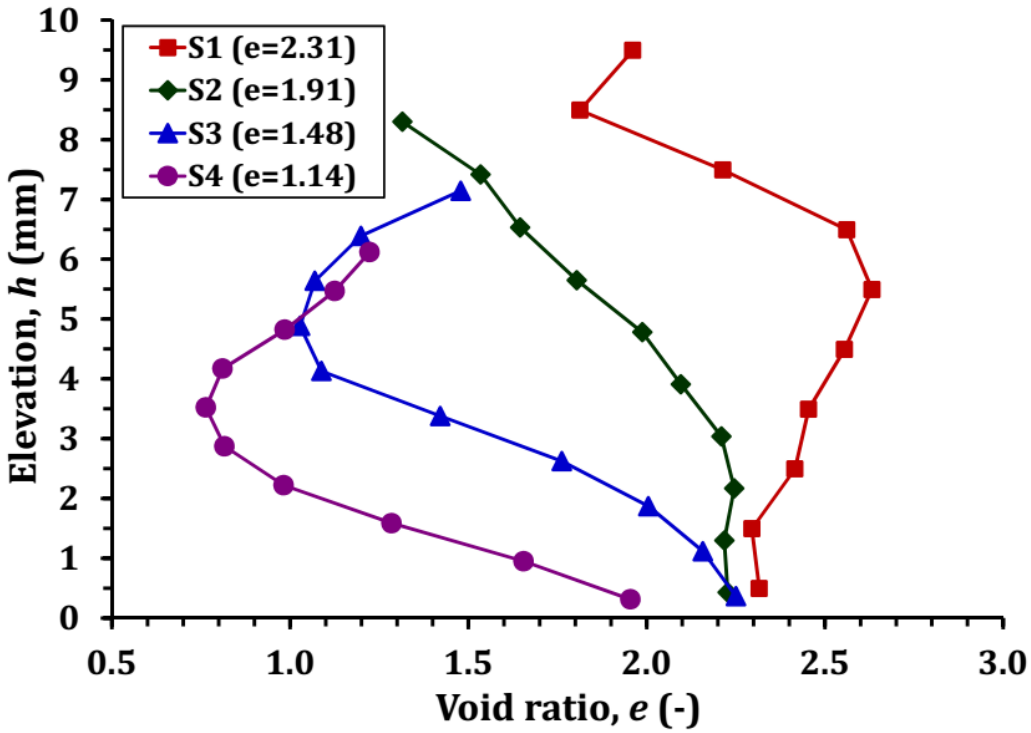

Figure 6: Void ratio versus elevation at different compaction levels. Note that the value in the parenthesis is the average void ratio.

In the initial state (S1 – red curve), the void ratio is largest at h = 5.5 mm ($e_{max} \approx 2.65$) because of the existence of several large pores in the center and the periphery of the specimen (see Figure 4*a*). Meanwhile the sample is denser at the bottom and densest at the top. The higher density at the bottom could be explained by a higher stress induced by the weight of the sample. The higher density at the top could be related to the preparation of the sample surface. Actually, after having filled the cell with wet grains, the excess grains on the top of the sample were removed to obtain a planar sample top surface. Even if this action was done with care, that would induce supplementary stress that slightly compacted the top layer of the sample. At the stage S2 (dark-green curve), the structure is notably compacted and rearranged; void ratio in the middle and at the top is significantly reduced. The structure in the middle is remarkably disturbed when passing the stage S2 to S3 (blue curve). At the densest state (S4 – dark-purple curve), a strong decrease of void ratio is obtained in the middle (e_{min} = 0.7) while the structure at the bottom is slightly rearranged.

3 Processing for local scan images

3.1 Principles

Based on the local scans, virtual cubical specimens (edge length = 1.95 mm) were extracted to analyze the grain-scale behavior of the sample during compression. Hereafter, these cubes are referred to as *Standard Volume*, or SV; one example is shown above in Figure 3*c*. Ten SVs were extracted at ten different positions (at the top, at the bottom, and in the central layers; and for each layer, at the periphery and at the center) in order to consider the sample microstructure heterogeneity. The subsets did not spatially overlap each other. It is worth to note that a much higher number of SV, extracted randomly, would be preferable but it would significantly increase the computational cost.

The algorithm used to detect spherical structures within 3D images, initially developed by Xie *et al.* [47] for 3D images, was used and modified following Peng *et al.* [48] (proposed for 2D images) along with the Adaptive Hough Transform algorithm of Illingworth & Kittler [49]. Note that this algorithm is not applicable for natural materials (i.e. sand grains) where more advanced methods are required [50, 51].

3.2 Algorithm for detecting spherical grains

The algorithm to detect spherical structures is illustrated in Figure 7. A 3D image with a cubic shape, and formatted as a 3D array, is first extracted from the local scans. The position of the center of the spheres is then directly located within the 3D array. Afterward, the radii of the spheres (with identified central position) are identified. Finally, the 3D reconstruction process and analysis are carried out based on the detected spheres.

The detailed description of the main algorithm (see dashed-red square in Figure 7) is given in the following subsections.

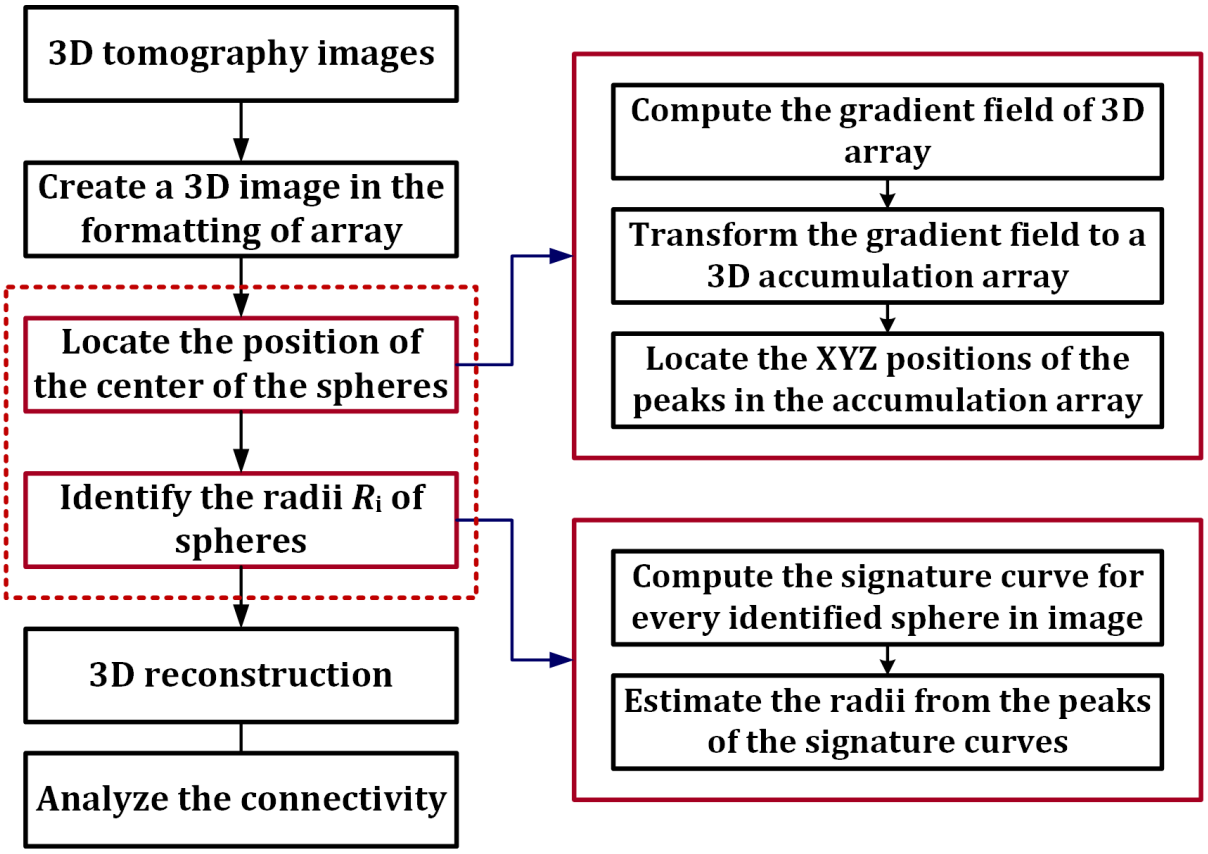

Figure 7: Algorithm used to detect the spherical structures.

3.2.1 Locating the center of the spheres

To compute the center's position of a sphere in the 3D image, the voxels that belong to that sphere are first identified, and then the centroid of those voxels is computed. The gradient field of image intensity is computed using the following equation:

$$\nabla \mathbf{I}(i,\ j,\ k) = (\boldsymbol{V_x}, \boldsymbol{V_y}, \boldsymbol{V_z})|_{(i,\ j,\ k)}$$

$$= (I(i,\ j,\ k) - I(i,\ j,\ k-1), I(i,\ j,\ k) - I(i,\ j-1,\ k), I(i,\ j,\ k) - I(i-1,\ j,\ k)),$$

(*Erreur ! Signet non défini.*)

where (i, j, k) are the voxel indices, $\nabla\mathbf{I}(i, j, k)$ is the gradient vector at voxel (i, j, k), which consists of x, y and z components, and $\mathbf{I}(i, j, k)$ is the image intensity at voxel (i, j, k).

In a gradient field, the nonzero gradient vectors are either pointing toward the center of a sphere or away from it. So, a transform is defined to convert the gradient field to an accumulation array, in which the voxel intensity corresponds to the probability of that voxel being the center of a sphere. The accumulation array, constructed by an additive process (see Figure 8), has the same dimension of the gradient field. In the accumulation image, the maximum intensity represents the center position of a sphere. In the gradient field, a weight value is added to the voxels which have a nonzero gradient vector $\nabla\mathbf{I}(i, j, k)$ in the accumulation array. The line segment in each direction is defined by the vector $\nabla\mathbf{I}(i, j, k)$. The length of the line segment is set to be the possible maximum diameter of the spheres, and the magnitude of $\nabla\mathbf{I}(i, j, k)$ is used as the weight value. The accumulation array is built from the collecting of all nonzero gradient vectors in all directions. In Figure 8, the darkest voxel has the maximum weight.

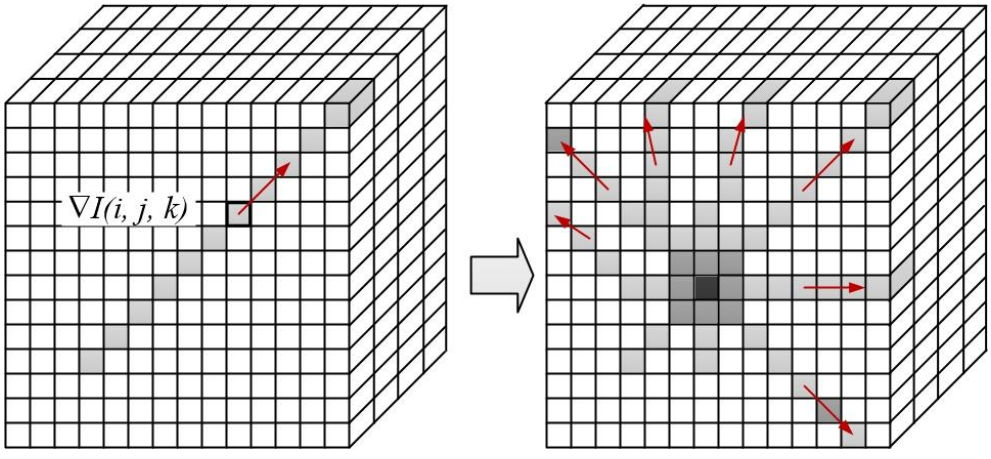

Figure 8: Construction of the accumulation array from the gradient field: the nonzero gradient vector added to the accumulation array (left), and the accumulation array after adding the nonzero gradient vectors in various directions (right).

3.2.2 Estimating the spheres' radius

In order to determine the spheres' radius, a signature function $f(r)$ is defined over the gradient field of the sphere's image, where r is the distance to the center position of the sphere and $f(r)$ is the averaged dot product of the gradient vector and the radial vector.

Figure 9 shows the definition of the signature function, in which (i_c, j_c, k_c) is the center position of a detected sphere. For a voxel (i, j, k) in the neighborhood of (i_c, j_c, k_c), $V(i, j, k)$ is the gradient vector of (i, j, k) and $q(i, j, k)$ is the vector joining (i_c, j_c, k_c) to the center of (i, j, k). A sequence of discrete r values with fixed interval is selected. It represents the distances to the center of the sphere (i_c, j_c, k_c). For each r value, $f(r)$ is defined by the following equation:

$$f(r) = \frac{\sum_{||\vec{q}(i,j,k)|-r|<\Delta r/2}[\vec{V}(i,j,k).\vec{q}(i,j,k)/|\vec{q}(i,j,k)|]}{\sum_{||\vec{q}(i,j,k)|-r|<\Delta r/2}\mathbf{1}}, \qquad \textbf{(Erreur ! Signet non défini.)}$$

where the sum is over all the voxels whose distance from (i_c, j_c, k_c) is within the range $[r - \Delta r/2, r + \Delta r/2]$.

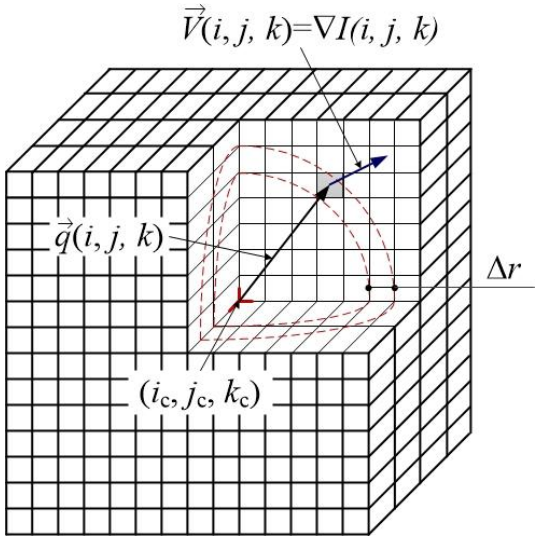

Figure 9: Definition of the signature function.

Figure 10 illustrates an example of the signature function. The radius of the sphere corresponds to the distance to the center presenting the highest value of *f*(r). In the example shown, the radius equals seven times the voxel size (*i.e.* 45.5 microns). Note that, in the present work, only rounded values of radius are considered.

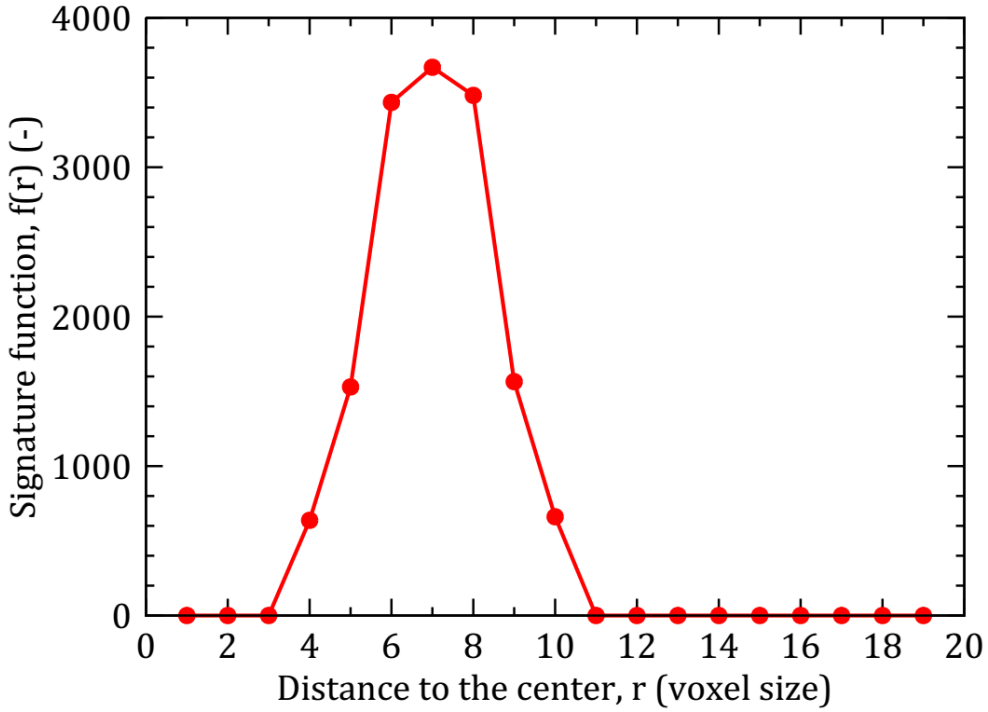

Figure 10: An example of signature function computed from the 3D image.

Figure 11 shows an example for one slice in a 3D image. The blue disks are the detected spheres, and the red points represent their centers. Incomplete white disks at the border are not used for the detection of the centers.

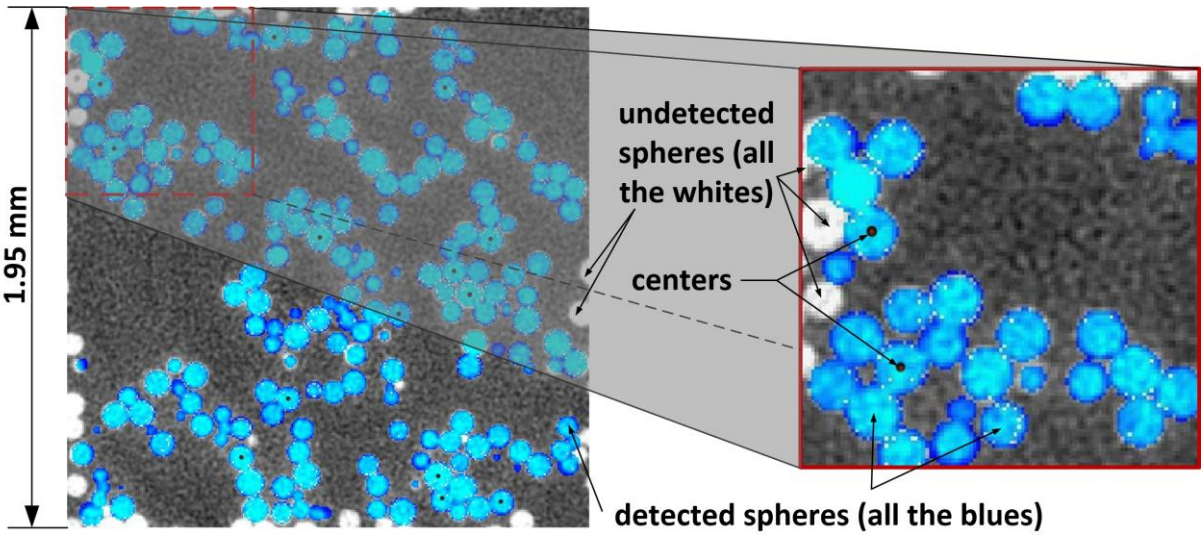

Figure 11: A slice in a 3D detected image.

3.2.3 Estimating the lost contacts after the detection process

As mentioned above, after the detection process, the spheres that intersect the border of the cube cannot be identified (Figure 11). Hence, the contacts between these spheres and their neighbors inside the SV cannot be considered. In order to estimate those lost contacts, a method is proposed as follows. A new cube which is larger than the SV is created. It is called the Extended Volume (or EV) with the edge length b (see Figure 12), $b = a + 2d_{max}$, where a is the edge length of the SV, d_{max} is the maximal diameter of the detected spheres. The EVs are then analyzed with the same input parameters and compared with the SVs. All grains inside the SVs and the EVs having the same coordinates are first identified. The grains, inside the EVs (but not identified with the SVs) can be then distinguished.

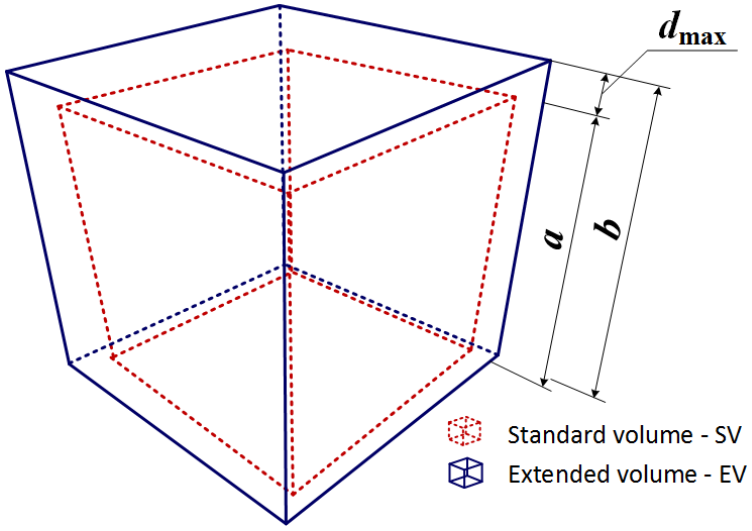

Figure 12: Method to find the lost contacts; the inner cube is the standard volume (SV) and the outer one is the extended volume (EV).

3.3 3D images reconstruction

Figure 13 illustrates an example of 3D images reconstruction for the SV before and after the detection. The specimens (a) and (b) are directly reconstructed from 3D tomography images, the small cube (b) being extracted from the specimen (a). The specimens (c) and (d) are reconstructed from 3D binary images. The specimen (e) is reconstructed from the exact positions of particles after the detection process. The small cubes (f) is extracted from (e). As the detected radius can only equal to rounded values of voxel size, a tolerance of 1 voxel size (6.5 microns that is 7.14 % of the average grains' diameter) is then added to the grains' diameter in order to better consider the error related to the detection process. With this correction, the images (e) and (f) become (g) and (h), respectively.

Figure 13*a* shows several large pores (up to 1 mm) and stacks of spheres having dimension ranging from 0.3 to 0.5 mm. As the average diameter of sphere is 100 micrometers, around 15 layers of voxels compose each sphere (as seen clearly in Figure 13*b*).

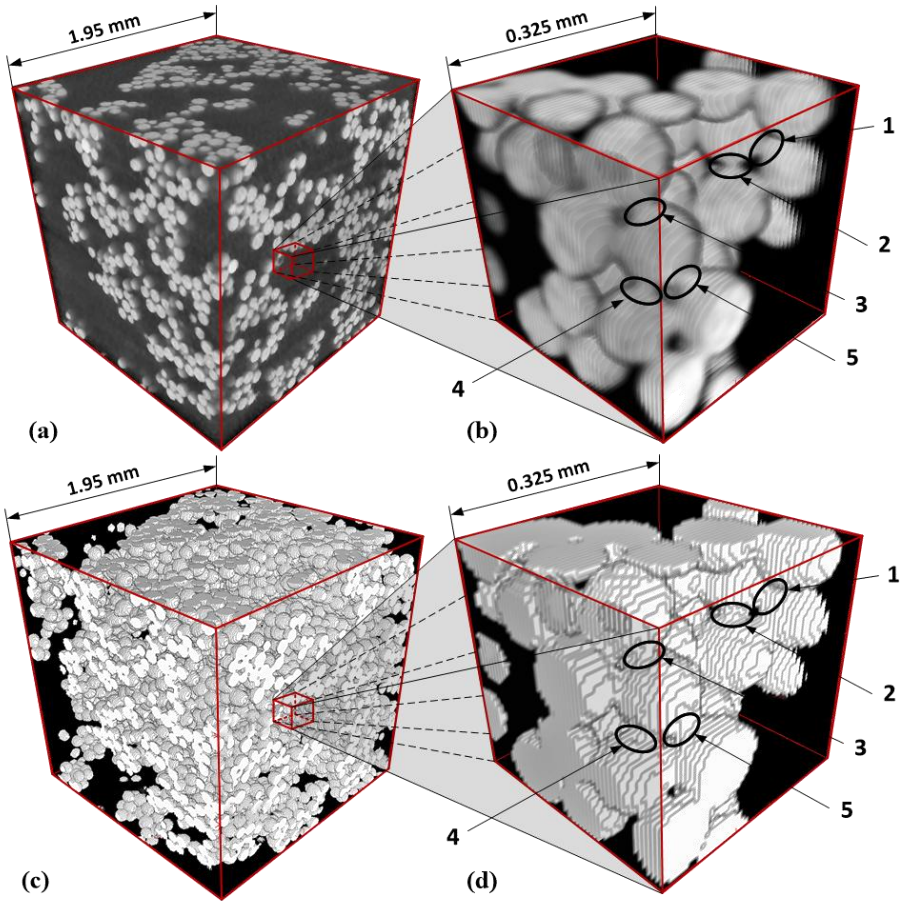

377

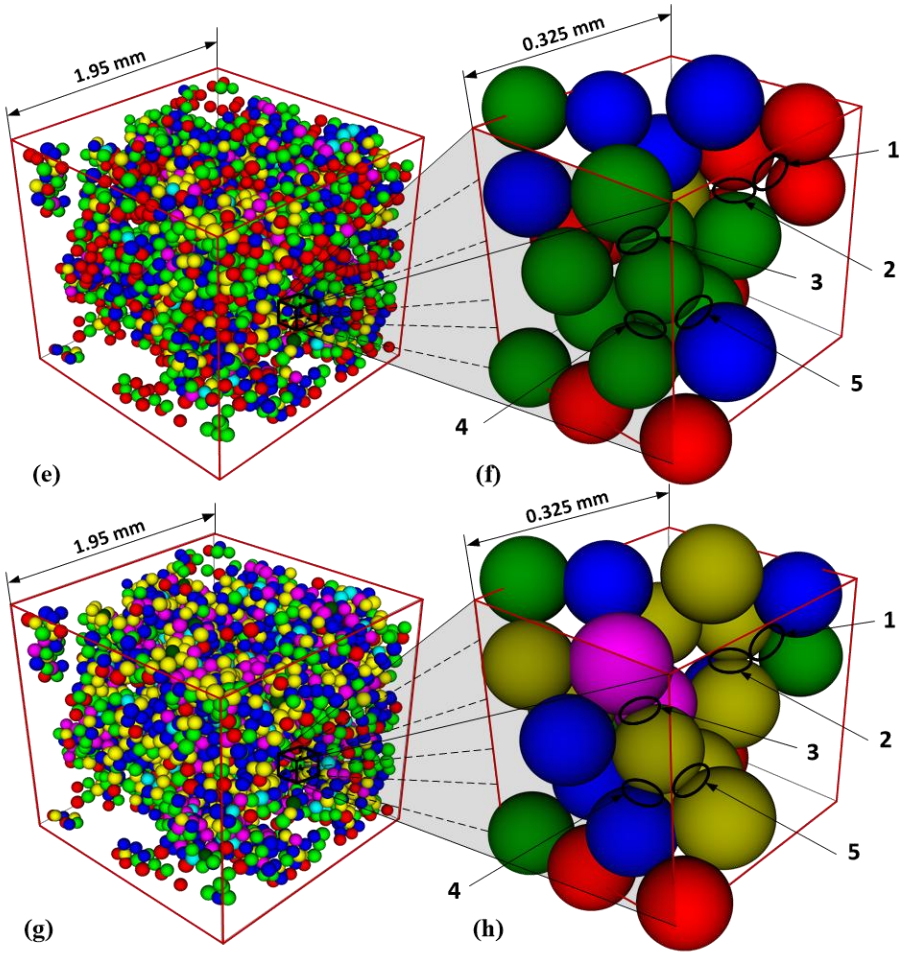

378

Figure 13: Example of reconstructed 3D specimens: (a, b) Original image - (c, d) Binary images of the investigated cube; (e, f) Reconstructed 3D image with tolerance of 0 voxel; (g, h) Reconstructed 3D image with tolerance of 1 voxel.

The contact between spheres is obvious in Figure 13(*b* and *d*). Some typical contacts are denoted by the positions 1 to 5. The corresponding spheres are kept in contact at these positions in the specimen after binarization (see Figure 13(*b* and *d*)). However, these spheres are no longer in contact after the detection process, as shown in Figure 13*f*. After adding a tolerance of 1 voxel size to the diameter of all spheres, these contacts appear to be similar to the ones observed before the detection. Clear evidence is shown in Figure 13*h*. In Figure 13(*e-h*), the color of spheres encodes their number of contacts as follows: the red, green, blue, yellow, magenta represent the spheres having zero, one, two, three, and four contacts, respectively. Comparison of Figure 13*f* and Figure 13*h* clearly shows the effect of the change of tolerance on the detected contacts.

The macroscopic solid fraction and the average solid fraction of ten SVs are illustrated in Figure 14. The “macro” values (red columns) are computed from the void ratio of the entire specimen (Figure 2). The green columns (BD) show the average values, which were directly calculated from the binary images (before detection). The results show that the macroscopic solid fraction is different from that estimated at the center of the specimen. That can be partly explained by the heterogeneity of the microstructure of the sample (as shown in Figure 4 and Figure 6). In addition, after the detection process, the solid fraction is computed by dividing the volume of all particles by the volume of the cube (blue columns). The solid fraction obtained after the detection process with zero tolerance (AD) is smaller than that before the detection. However, with one voxel size tolerance (AD-Tol1), the results (magenta columns) are very close to the ones before detection (green columns). This suggests that the use of a

tolerance of one voxel size for all analyses of the 3D images after the detection process is quite suitable. For this reason, in the following analyses, only the detection results with tolerance of one voxel size are considered.

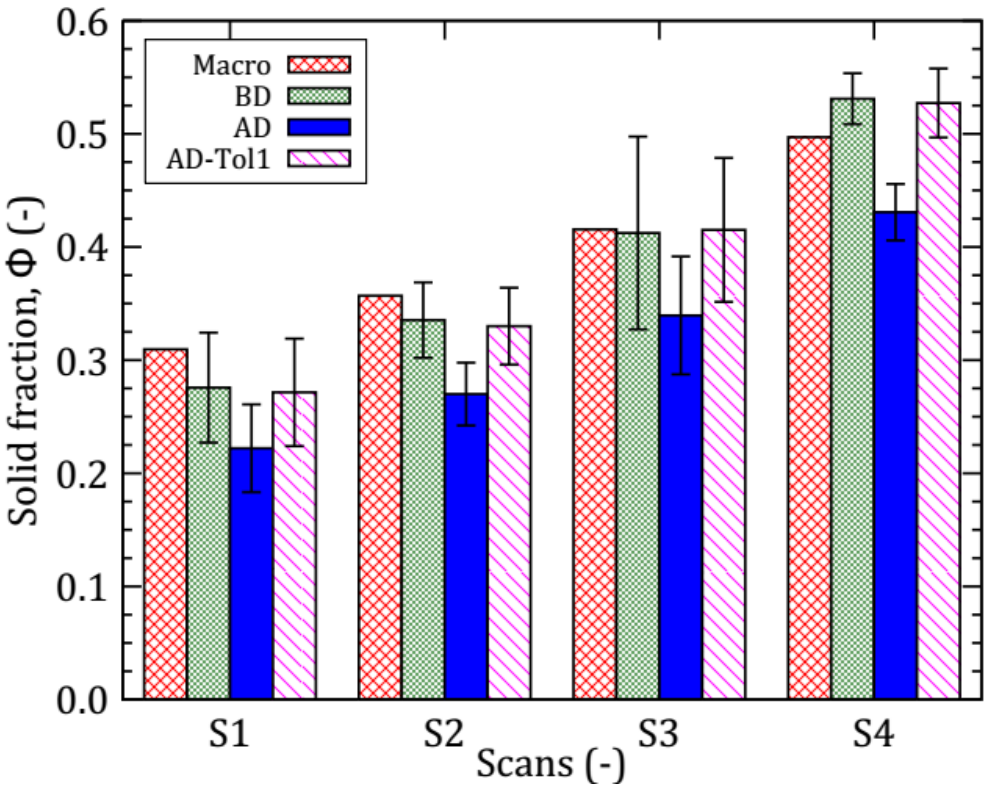

Figure 14: Solid fraction at different compaction levels. AD denotes after detection, BD denotes before detection.

4 Pore-scale characterization

In this section, the pore-scale deformation of specimen under growing of compaction level is characterized via the pore-distance distribution. To obtain this distribution, a large quantity of points (about fifty times the number of particles) is randomly placed into the pore space of the specimen. For each point, the shortest distance from this point to a grain is then identified. In other words, this distance is the radius of a "virtual" sphere which has this point as its center and has one contact point with a "real" grain. The cumulative probability of the identified

421 distances is then computed. A statistic of the identified distances is finally collected in the
422 form of a cumulate probability. The pore distance distribution of the specimen at four
423 compaction levels is illustrated in Figure 15 in which the distance is normalized by the
424 average diameter $\langle d \rangle$ as the following equation:

425 $$\langle d \rangle = \frac{2 d_{\max} d_{\min}}{d_{\max} + d_{\min}}. \quad (1)$$

426 Here, $d_{\max}$ and $d_{\min}$ are the maximal and minimal diameters of grains, respectively.

427

428 In Figure 15, at each compaction level, the gold region denotes the range of pore distance
429 distribution (for briefness, hereafter in the section referred to as the gold region) of ten
430 different positions (ten cubes SV) in the specimen, and the continuous line denotes the
431 average value of these ten distributions. In general, the pore distances strongly decrease, $R_{\max}$
432 $\approx 4\langle d \rangle$ in S1 reduces to $R_{\max} \approx \langle d \rangle$ in S4, under growing of compaction level. In the loosest
433 state S1 (Figure 15*a*), the gold region is rather large. That means the pore structure of the ten
434 SVs is different from each other. For instance, the pore having size $R \leq \langle d \rangle$ occupies
435 approximately 40 % at the lowest boundary while its percentage is about 99 % at the highest
436 boundary and is about 80 % for the average value; the very large pores, $R \geq 3\langle d \rangle$, still occupy
437 a remarkable quantity (7 %) at the lowest boundary. An example of several large pores can be
438 clearly seen in Figure 13*a*. In the denser states S2 and S3 (Figure 15(*b* and *c*)), the pore
439 distance distributions significantly decrease, $R_{\max}$ reduces to approximately $2\langle d \rangle$. In the
440 densest state S4 (Figure 15*d*), the gold region is rather small. This means that the pore
441 distance distribution of the ten SVs is rather similar in this state. The pore distances decrease
442 twofold from the state S3, $R_{\max} \approx \langle d \rangle$. In addition, 99 % of the pores have a radius smaller
443 than $0.5\langle d \rangle$ and 50 % smaller than $0.1\langle d \rangle$ in average. It should be noted that the pore
444 distribution shown in Figure 15 corresponds to that of the ten SVs, the large voids observed in
445 larger scale (Figure 4) are not considered. To assess the pore distribution of the whole
446 specimen (shown in Figure 4), the binary x-ray 3D images can be used.

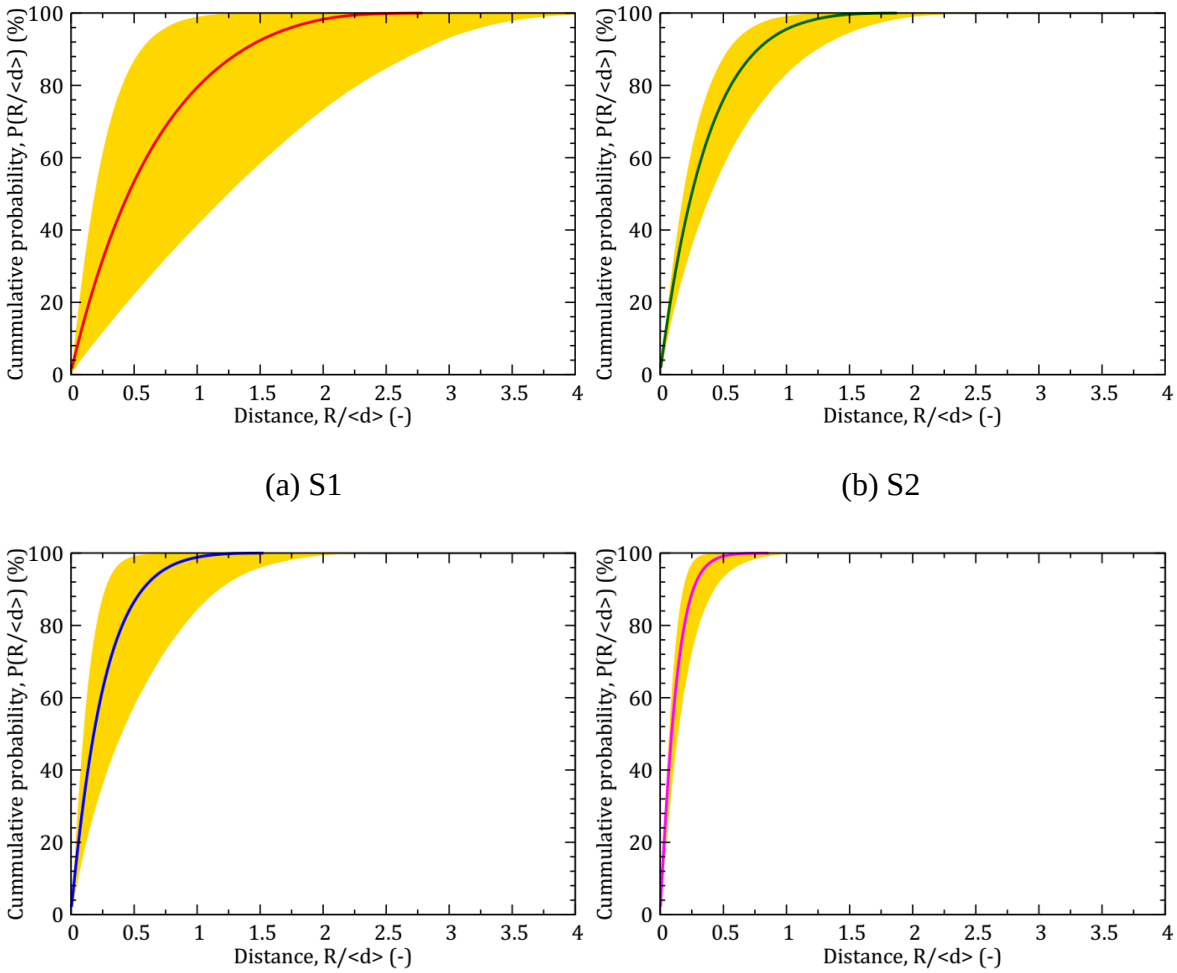

Figure 15: Pore distance distribution for four compaction levels. In each level, gold region denotes the values of ten cubes; continuous line denotes the average value.

5 Grain-scale analysis

The 3D reconstructed images are used in this section to perform grain-scale analysis in the SVs. As mentioned above, the agreement in solid fraction (Figure 14) suggests that the use of a tolerance of one voxel size for all analyses of the 3D images after the detection process is quite suitable. In this section, only the 3D reconstructed images with tolerance of one voxel size are considered.

5.1 Total coordination number

In granular materials, the coordination number z is defined as the average number of force-carrying contacts per grains. If N_C is the number of force-carrying contacts between N grains, then the coordination number is $z = 2N_C/N$. In the present analysis, N_C is redefined as the number of pairs of contacts between N grains. Pairs of contacts mean two particles that have a distance between the two centers smaller than or equal to the sum of their radii. Therefore, in the present part, z is called the total coordination number.

Figure 16 plots the average total coordination number z for the four compaction levels, S1 to S4. The error bar denotes the standard deviation of ten values of ten SVs at each scan. In the loosest state S1, z equals to 5.29; it increases at higher density and reaches to 5.83 at the densest state S4. z remarkably varies at higher density (see the error bars in Figure 16). This means that z is significantly different in the ten SVs. In other words, the average value of z considerably depends on the structure of the specimen. As already shown in Figure 6, under growing of compaction level, the void ratio in the central elevation decreases nearly twofold (in the states S3 and S4) while it is negligibly decreased at the bottom elevation. This reflects a strong rearrangement of the structure. In other words, the central zone of specimen is denser than the bottom and the top ones. This explains why the z varies more largely in the states S3 and S4.

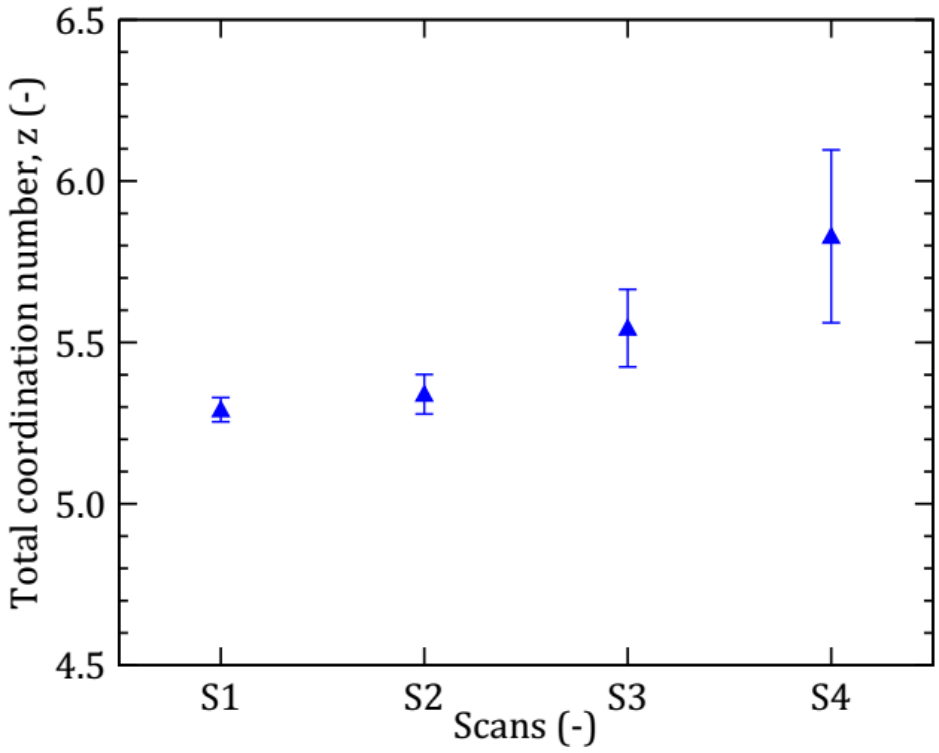

Figure 16: Average total coordination number for different compaction levels.

5.2 Coordination number of close neighbors

The coordination number of close neighbors, $z(h)$, is the average number of neighbors of one particle separated by an interstice narrower than h. The interparticle distance h can be normalized by the average diameter $\langle d \rangle$. Figure 17 shows, for the four compaction levels, $z(h)$ versus the interparticle distance between grains; this distance varies between 0 and 1 voxel size (that is $0 \leq h/\langle d \rangle \leq 0.07$). The color region represents the variation of ten SVs, the continuous line represents the average value. At $h = 0$, $z(h = 0)$ is equal to z (see Figure 16). At the loosest state S1, $z(h)$ increases from 5.29 to 5.75 (about 9 %) while it increases from 5.83 to 7.16 (approximately 23 %) at the densest state S4. Actually, this increased rate reflects the structure of the specimen. This can be explained via the decrease in the pore distance distribution, as depicted in Figure 15. Under growing of compaction level, when the specimen is compressed, the large pores are strongly decreased (*e.g.* $R_{max}/\langle d \rangle$=4 downs to $R_{max}/\langle d \rangle$=1, from the S1 to the S4). This means that the specimen becomes denser. That explains why the

number of close neighbors at the denser states increases more quickly than the one at the looser states. In addition, similar to z, the variation of $z(h)$ at the denser states is larger than the one at looser states.

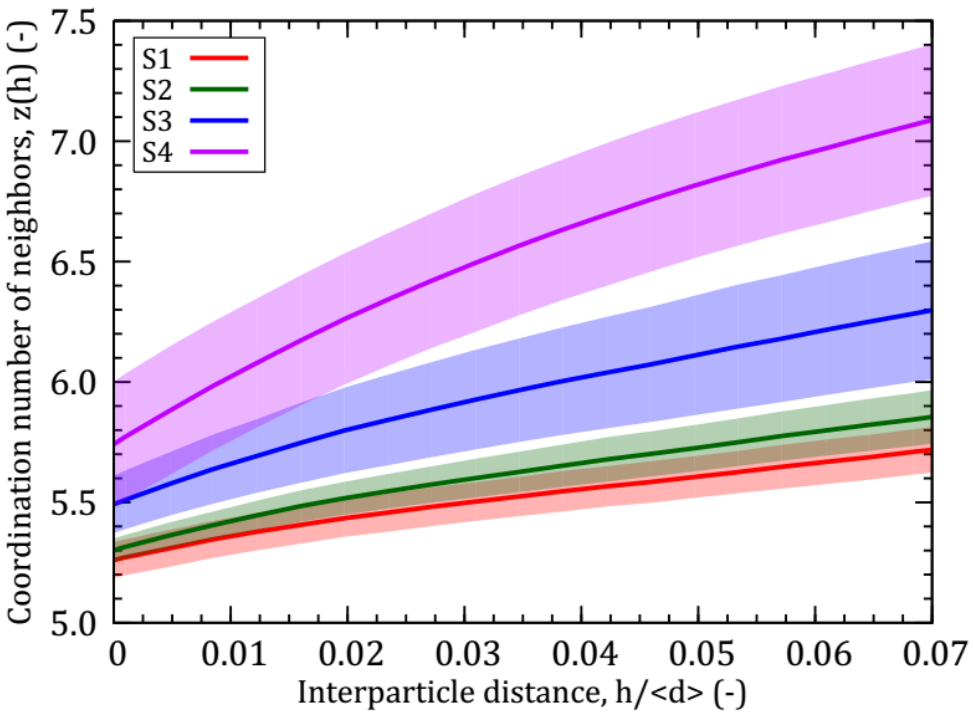

Figure 17: Average coordination numbers of close neighbors for different compaction levels.

5.3 Number of contacts per grain

Figure 18 shows the average number of contacts per grain for the four compaction levels. In general, the grains have zero contact to eleven contacts, and the fraction of grains having two or three contacts are predominant, *i.e.* 20 - 24 % for each of these categories. For the denser state, the occurrence of high values of N_C ($N_C \geq 3$) is higher than in the other states while at low value of N_C ($N_C < 3$), this occurrence is lower than in the looser states. This confirms the influence of the granular structure on the contacts of grains. Under growing of compaction level, the specimen's structure becomes denser and more contacts are created. Theoretically, the maximal number of contacts per grain is 12. In the present case, $N_C = 11$ is the maximal

value and it occupies a minimal probability, nearly 0.003 % (S3) and 0.007 % (S4). This probability only occurs in the denser states (S3 and S4) and it is equivalently a few grains having 11 contacts. N_C = 0 still occupies a significant percentage, approximately 9.0 % to 9.5 %. In reality, the grain having zero contact does not exist in the granular structure. However, in the present case, a remarkable quantity of the grains having zero contact appears after the detection process.

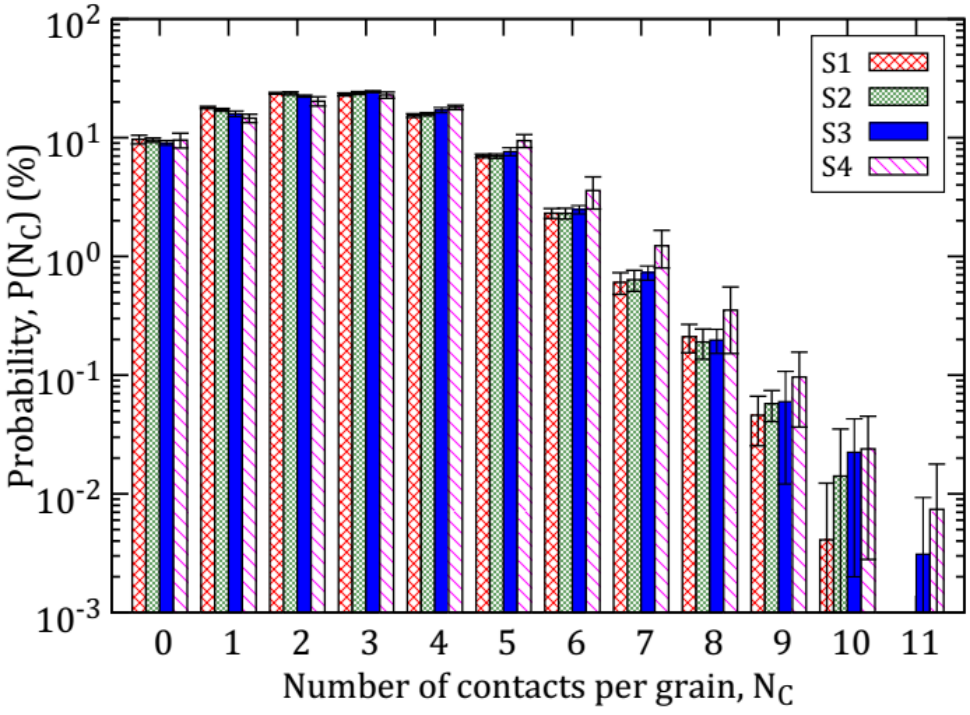

Figure 18: Average number of contacts per grain for different compaction levels.

Interestingly, spheres with one contact can be found in this structure, one example is illustrated in Figure 19. This is a small cube extracted from the Figure 13*a*. For these cases, after the detection process, these spheres have either one or zero contact. The presence of water menisci and the possible rolling resistance [52] at contact between grains could explain this. Indeed, with an average diameter of 100 microns, the particle weight loses relevance with respect to capillary forces [53], which could alone stabilize these grains. Besides, as the

surface of the grain is not really perfect (see Figure 1), the rolling resistance can be significant.

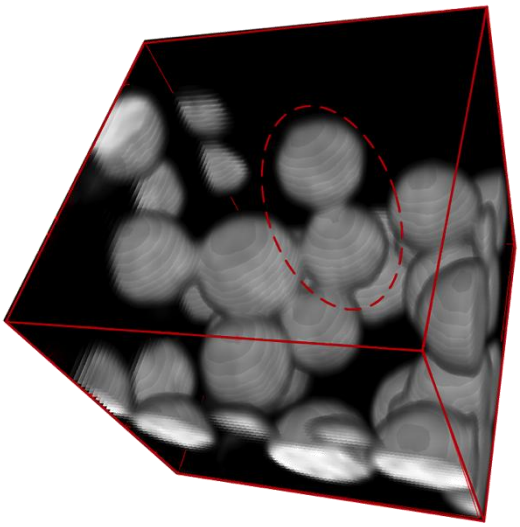

Figure 19: An example of a sphere having one contact.

5.4 Radial distribution function

The radial distribution function, $g(r)$, is the probability of finding a particle center in a spherical shell of a radius r, given that there is another particle at the center of the spherical shell [54]. $g(r)$ is related to the average number of particles by

$$p(r_2) - p(r_1) = \int_{r_1}^{r_2} g(r)\, 4\pi r^2 dr \,, \qquad \textbf{(Erreur ! Signet non défini.)}$$

where $p(r)$ is the average number density of particles in a spherical shell of radius r. In this formula, radial distances are normalized by the average diameter $\langle d \rangle$ (given by Eq. (3)).

Figure 20 shows $g(r)$ for the four compaction levels. The radial distance is normalized by the average diameter $(r/\langle d \rangle)$. The curves for the various states are nearly similar in their oscillations and peaks. $g(r)$ starts from a maximum value at $r = \langle d \rangle$ with different amplitudes; the loosest system presents the highest amplitude. $g(r)$ then decreases to minimum probability

at $r = 1.2\langle d \rangle$, $r = 1.3\langle d \rangle$, $r = 1.35\langle d \rangle$, and $r = 1.4\langle d \rangle$ for S1, S2, S3, and S4, respectively. It increases subsequently to a local peak at $r \approx 1.9\langle d \rangle$. From this peak, $g(r)$ continues to fluctuate slightly until it approaches a rather constant value at $r = 3.0\langle d \rangle$.

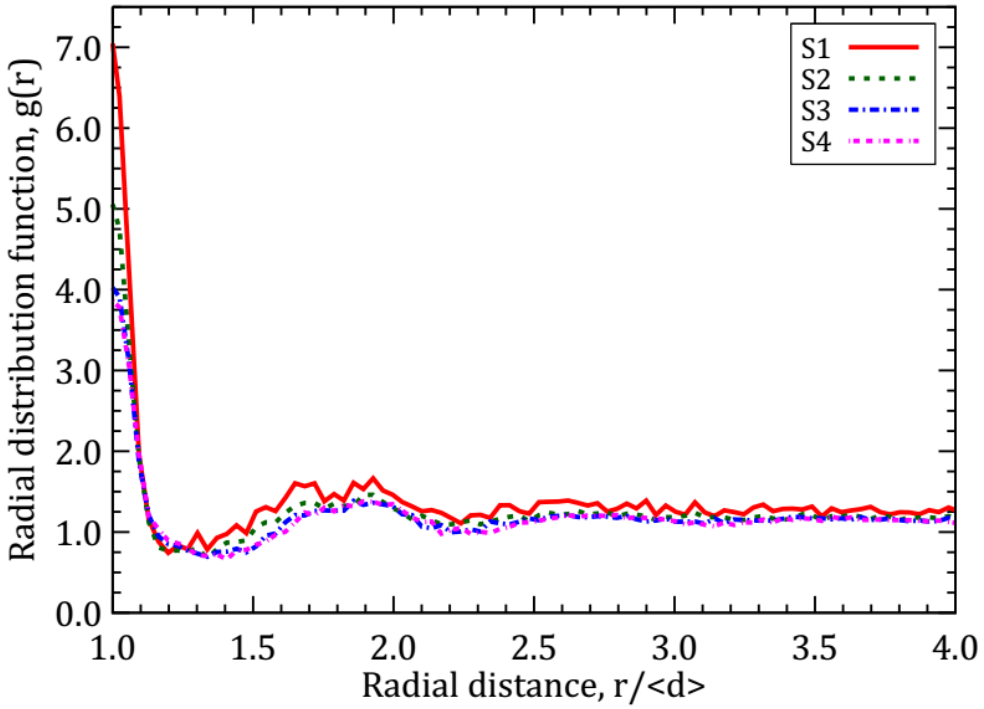

Figure 20: Radial distribution functions for particle centers of four compaction levels.

$g(r)$ is a useful tool to describe the structure of a system, and it has been used widespread in the study of granular materials, especially in the numerical simulations [55, 56]. At very short r ($r/\langle d \rangle < 1$) $g(r)$ must equal zero, because two particles cannot occupy the same space. It is clear that $g(r)$ should go to 1 for large r. $g(r)$ shown in Figure 20 goes indeed asymptotically to 1 for large r. As mentioned above, these analyses are performed on the ten SVs (virtual cubical specimens with edge length = 1.95 mm). At this scale, the results would suggest a representative volume element (RVE) size of about 3d (300 micron). However, characterization of the sample's homogeneity, based on the asymptotic behavior method for air and solid fractions [57], would give a better knowledge on the heterogeneity of the whole specimen (10 mm in height and 20 mm in diameter).

5.5 Contact network

Figure 21 illustrates the contact networks (on the left-hand side) and the reconstructed 3D image (on the right-hand side) of a typical SV (for each compaction level) represented in a narrow slice having a thickness of three times the grain diameter ($3\langle d\rangle \approx 40$ voxel sizes). The contacts between particles are represented by segments of different colors joining particle centers in two types (on the left-hand side of Figure 21): (*i*) the red lines link the center of two spheres in contact; (*ii*) the blue lines link the center of two spheres having an interparticle distance higher than zero but smaller than 1 voxel size (6.5 microns).

Under the lowest compaction level S1, structure exhibits strands (or chains) of single particles – see the rectangle regions of Figure 21(*a* and *b*). These chains still appear in the higher compaction level S2 (Figure 21(*c* and *d*)). This could be explained by the appearance of rolling resistance at contacts between grains as mentioned above. This resistance tends to react the collapse of structure under external applied forces. However, under higher compaction levels, these contacts are broken and the specimen is restructured; The chains of single particles no longer exist (see Figure 21(*e*-*h*)). This phenomenon is also observed in a numerical study of model cohesive grains using discrete element method [58].

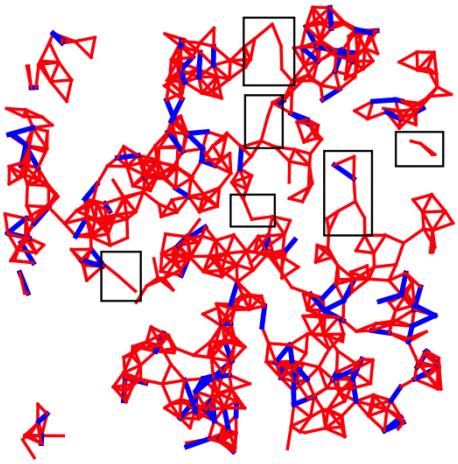

(a) S1

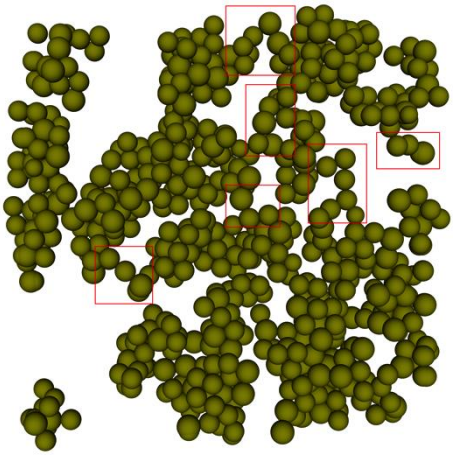

(b) S1

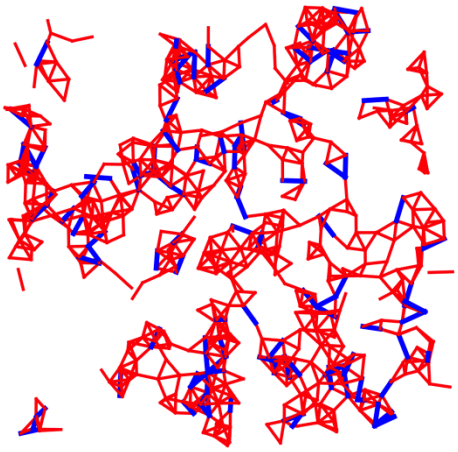

(c) S2

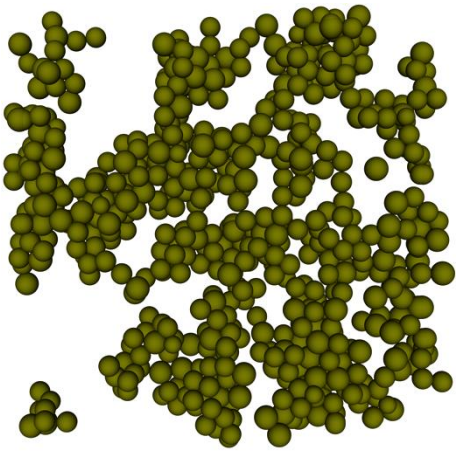

(d) S2

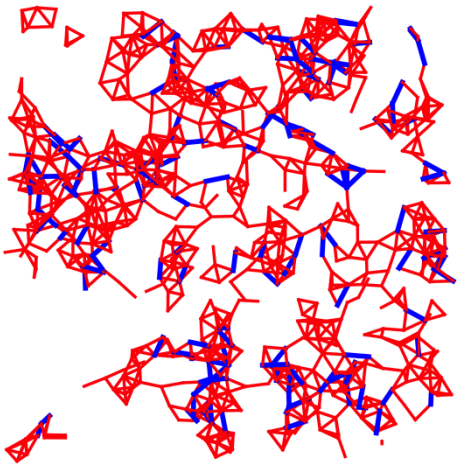

(e) S3

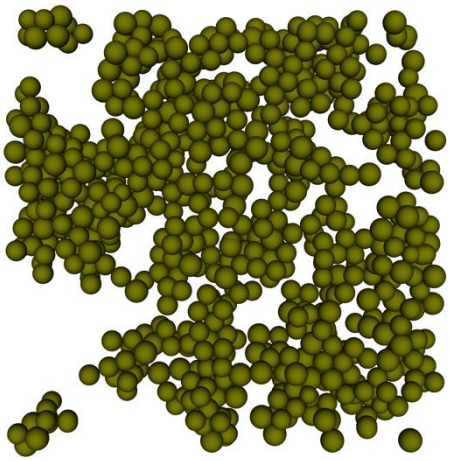

(f) S3

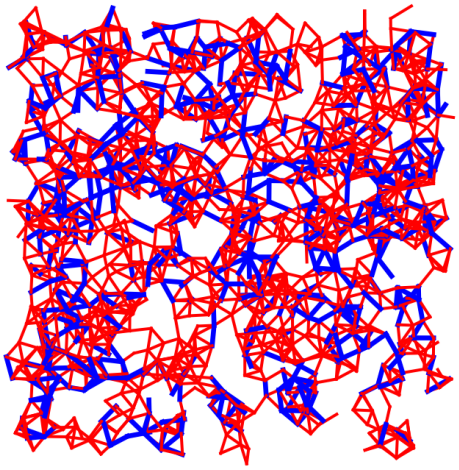

(g) S4

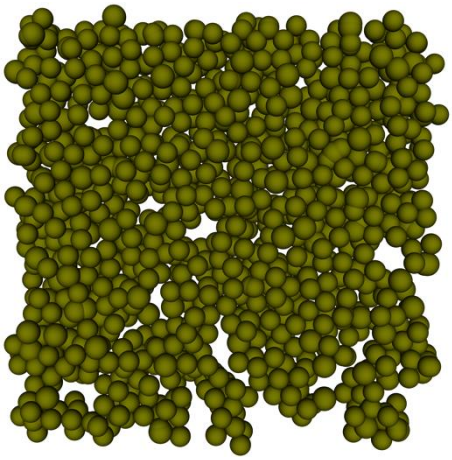

(h) S4

Figure 21: Contact network and reconstructed 3D image of a typical slice under growing of compaction level.

6 Discussion

A very loose yet stable-state of wet granular material was produced in laboratory even using very small water content. Evidently, the structure of the specimen is heterogeneous but it seems very difficult to make the specimen more homogeneous using such a low density.

The compression curves obtained show a 3-stages shape (see Figure 2). Following the usual concept of soil mechanics [5, 59], there are only two stages 1 and 2 on the oedometric compression curve. Interestingly, the stage 3 is also described in the S-shape curves obtained on agricultural soils [59]. In this stage, the void ratio is slightly decreased and maintained nearly constant at high stress (see Figure 2). That confirms the remarkable effect of the elastic deformation of grains at the contact points.

In the work of Than *et al*. [12], numerical simulations (by the discrete element method) of a model granular assembly, made of spherical balls, were used to investigate the influence of a small amount of an interstitial wetting liquid, forming capillary bridges between two adjacent particles on the plastic response in isotropic compression. The study was restricted to the pendular state of low saturation (degree of saturation smaller than 1%), in which the wetting liquid is confined in bonds or menisci joining contacting grains. By using glass beads of 115 µm (similar to those in the present work), a loose granular structure (void ratio equals 2.30) was created. Isotropic compression behavior of this structure showed equally a 3-stages shape. The agreement between the results obtained by the two methods (experiments in the present works and numerical simulation in the work of Than *et al*. [12]) confirm the key role of water menisci that stabilize the structure of specimen at very loose state. This statement is also in agreement with the results of Scheel *et al*. [41] showing a sharp rise of tensile strength of assemblies of wet glass spheres at very small water content.

In the present work the position and radius of the spheres were detected by the algorithm initially developed by Xie *et al.* [47] for 3D images, modified following Peng *et al.* [48] (proposed for 2D images) along with the Adaptive Hough Transform algorithm of Illingworth & Kittler [49]. Within this method, integer number of pixels was used to set the radius of particles, which would induce error on the characterization of the interparticle contacts. The results would be significantly improved by using the kalisphera-based technique [33] for sphere-matching in real 3D images of spheres. Besides, detecting interparticle contacts from x-ray microtomography 3D images by using a greyscale threshold that selects the correct solid volume would induce also error [60]. For the sake of simplicity, in the present work, the contacts were detected from the re-constructed 3D images and the above limitations should be considered when assessing the results.

633 The main contribution of the present work would be the links between macro and microscopic
634 behaviors of specimen under growing of compaction level (Figure 2, Figure 6, Figure 14-
635 Figure 17). In the stage 1 of the compaction curve (Figure 2), the void ratio remains nearly
636 constant and slightly decreases at the end of this regime (equivalently the position of the scan
637 S1). Under growing of stress in stage 2, the specimen structure quickly collapses. This is
638 evidently reflected by a twofold increase in solid fraction from the loosest state (S1) to the
639 densest state (S4) (see Figure 14) or by a twofold decrease of void ratio in the central layers of
640 the specimen (see Figure 6). Besides, the strong decrease in the pore distance distributions at
641 four compaction levels (see Figure 15) appropriately demonstrates this collapse. In the state
642 S3, the structure is significantly disturbed. This is obviously confirmed via the largest error
643 bar of solid fractions at the S3 (see Figure 14), the large gold region (see Figure 15*c*) and the
644 void ratio distribution (blue curve in Figure 6). At higher densities, the number of contacts is
645 larger than the one at lower densities (see Figure 16). In the stage 3 of the compaction curve,
646 starting from S4, the structure collapses negligibly because of the elastic deformation of
647 grains at contact regions. This is demonstrated by the highest density of S4 and the slight
648 increase of z (see Figure 16 and Figure 17).
649
650 Moreover, the pore-scale deformation of specimen under growing of compaction level is
651 clearly observed in Figure 15 and Figure 21. Initially, the structure can be stabilized in very
652 loose state with a significant quantity of very large pores (see Figure 15*a* and Figure 21(*a* and
653 *b*)). Several marked rectangle regions in Figure 21(*a* and *b*) show chains of single particles.
654 Such a structure cannot exist and stabilize without rolling resistance at contacts [58]. Under
655 growing of compaction level the structure quickly collapses and the pores size remarkably
656 decreases. In the densest state S4, the pores having size $R \geq 0.5\langle d \rangle$ (equivalently the grain
657 size) occupy a tiny amount (see Figure 15*d*), and they can be seen in Figure 21(*g* and *h*).
658

Concerning the grain-scale investigations, several authors reported the distribution of number of contacts (*i.e.* the coordination number) [27, 35, 61–63] by using different methods to detect the contacts between the spheres. However, calculating the number of contacts is difficult due to the uncertainty when calculating the accurate position of the center of the particle, especially with the small size of grains and low resolution of the tomography images. That is why the tolerance of 1 voxel size is chosen for all calculations in the present study. This tolerance is very close to the interval tolerance of $(1\text{-}2)^{1/3}$ voxel sizes used by Aste *et al*. [34, 62] while their size of particles is bigger than that in the present work and the resolution is not too much different. In several packing studies [35, 38, 62], the spheres are in contact with 11 particles at most and with 2 at least. Meanwhile, in the present study, the maximum number of contacts per grains is also 11 with a tiny percentage (0.03 % and 0.07 %) but this maximum value only occurs in the denser states. Besides, there is still a significant percentage of spheres that have zero (around 9.5 %) contact which should not exist theoretically. As mentioned previously, the rounded values of the detected spheres remarkably affect the accuracy of these analyses.

7 Conclusion

A very loose structure of granular materials (glass beads) is experimentally created thank to the presence of a small quantity of water forming capillary bridges. One-dimensional compression tests combined with X-ray computed tomography observations allow addressing the following conclusions:

Firstly, the macroscopic behavior of wet beads at loose state (initial void ratio of about 2.30) obtained from oedometric compression tests has usually three regimes: (*i*) at stresses lower than the apparent pre-compression stress, the initial structure sustains the applied load with a very small rearrangement; (*ii*) when the stresses exceed the pre-compression stress, the loose

structures collapse and restructure; and (*iii*) at higher stresses, the elastic deformation of grains at contact points dominates the specimen deformation. The XRCT observations (global scans) show that the initial loose structure is heterogenous, consisting of large voids, and its behavior during the second regime is mainly related to the structure rearrangement around these large voids.

Second, the position and radius of the spheres were detected by combining various algorithms proposed in the literature. Within this method, integer number of pixels was used to set the radius of particles. From the 3D reconstructed images, several fundamental microstructural properties are obtained such as coordination number, number of close neighbors, distribution of number of contacts, radial distribution function, contacts network. Changes of these properties at various stages of the compression curve allow better understanding the main mechanisms at grain-scale level that influence the behavior at the pore scale and the macroscopic scale. Although this experimental approach still needs to be improved, in comparison with some existing numerical and experimental works, it provides an appropriate characterization of the grain-scale behavior of wet granular soils at very loose states during compression.

Finally, our results emphasize the key role of water menisci that stabilize the structure of specimen at very loose state as well as the appearance of rolling resistance at contact between grains. Indeed, the intrinsic compression behavior is due to the collapse of pore's structure and the rearrangement of grains in the specimen under growing of external force.

Acknowledgements

710 This work is part of the first author's Ph.D. thesis funded by the Ministry of Education and
711 Training of Vietnam. The authors are grateful to Dr. Michel Bornert (Laboratoire Navier) for
712 his useful suggestions and Mr. Jean-Marc Plessier (Laboratoire Navier) for the scanning
713 electronic microscopic image of a glass bead.
714

715 **References**

716 1. Wood DM (1990) Soil behaviour and critical state soil mechanics. Cambridge University
717 Press
718 2. Mitchell JK, Soga K (1976) Fundamentals of Soil Behavior. Wiley
719 3. Pierrat P, Caram HS (1997) Tensile strength of wet granular materials. Powder Technol
720 91:83–93. doi: 10.1016/S0032-5910(96)03179-8
721 4. Fournier Z, Geromichalos D, Herminghaus S, et al. (2005) Mechanical properties of wet
722 granular materials. J Phys Condens Matter 17:477–502. doi: 10.1088/0953-
723 8984/17/9/013
724 5. Munõz-Castelblanco J, Delage P, Pereira J-M, Cui YJ (2011) Some aspects of the
725 comression and collapse behaviour of an unsaturated natural loess. Géotechnique Lett
726 1:17–22. doi: 10.1680/geolett.11.00003
727 6. Jiang M, Hu H, Liu F (2012) Summary of collapsible behaviour of artificially structured
728 loess in oedometer and triaxial wetting tests. Can Geotech J 1157:1147–1157. doi:
729 10.1139/T2012-075
730 7. Mitarai N, Nori F (2006) Wet granular materials. Adv Phys 00:1–50.
731 8. Bruchon J-F, Pereira J-M, Vandamme M, et al. (2013) Full 3D investigation and
732 characterisation of capillary collapse of a loose unsaturated sand using X-ray CT. Granul
733 Matter 15:783–800. doi: 10.1007/s10035-013-0452-6
734 9. Mason TG, Levine AJ, Ertaş D, Halsey TC (1999) Critical angle of wet sandpiles. Phys
735 Rev E 60:R5044–R5047.

736 10. Delenne J-Y, El Youssoufi MS, Cherblanc F, Bénet J-C (2004) Mechanical behaviour and
737 failure of cohesive granular materials. Int J Numer Anal Methods Geomech 28:1577–
738 1594. doi: 10.1002/nag.401
739 11. Delenne J-Y, Soulié F, El Youssoufi MS, Radjai F (2011) From liquid to solid bonding in
740 cohesive granular media. Mech Mater 43:529–537. doi: 10.1016/j.mechmat.2011.06.008
741 12. Than V-D, Khamseh S, Tang A-M, et al. (2016) Basic Mechanical Properties of Wet
742 Granular Materials: A DEM Study. J Eng Mech C4016001. doi:
743 10.1061/(ASCE)EM.1943-7889.0001043
744 13. Sweijen T, Nikooee E, Hassanizadeh SM, Chareyre B (2016) The Effects of Swelling and
745 Porosity Change on Capillarity: DEM Coupled with a Pore-Unit Assembly Method.
746 Transp Porous Media 113:207–226. doi: 10.1007/s11242-016-0689-8
747 14. Sweijen T, Chareyre B, Hassanizadeh SM, Karadimitriou NK (2017) Grain-scale
748 modelling of swelling granular materials; application to super absorbent polymers.
749 Powder Technol 318:411–422. doi: https://doi.org/10.1016/j.powtec.2017.06.015
750 15. Chalak C, Chareyre B, Nikooee E, Darve F (2017) Partially saturated media: from DEM
751 simulation to thermodynamic interpretation. Eur J Environ Civ Eng 21:798–820. doi:
752 10.1080/19648189.2016.1164087
753 16. Melnikov K, Wittel FK, Herrmann HJ (2016) Micro-mechanical Failure Analysis of Wet
754 Granular Matter. Acta Geotech 11:539–548.
755 17. Delenne J-Y, Richefeu V, Radjai F (2015) Liquid clustering and capillary pressure in
756 granular media. J Fluid Mech 762:R5-1-R5-10. doi: 10.1017/jfm.2014.676
757 18. Gilabert F, Roux J-N, Castellanos a. (2008) Computer simulation of model cohesive
758 powders: Plastic consolidation, structural changes, and elasticity under isotropic loads.
759 Phys Rev E 78:031305. doi: 10.1103/PhysRevE.78.031305
760 19. Kadau D, Bartels G, Brendel L, Wolf DE (2003) Pore Stabilization in Cohesive Granular
761 Systems. Phase Transitions 76:315–331. doi: 10.1080/0141159021000051460

762 20. Khamseh S, Roux J-N, Chevoir F (2015) Flow of wet granular materials: a numerical
763 study. Phys Rev E 92:022201–19. doi: 10.1103/PhysRevE.92.022201
764 21. Richefeu V, Radjaï F, Youssoufi MS El (2006) Stress transmission in wet granular
765 materials. Eur Phys J E 21:359–369.
766 22. Richefeu V, El Youssoufi MS, Azéma E, Radjaï F (2009) Force transmission in dry and
767 wet granular media. Powder Technol 190:258–263. doi: 10.1016/j.powtec.2008.04.069
768 23. Rognon PG, Roux J-N, Wolf D, et al. (2006) Rheophysics of cohesive granular materials.
769 Europhys Lett 74:644–650. doi: 10.1209/epl/i2005-10578-y
770 24. Scholtès L, Chareyre B, Nicot F, Darve F (2009) Micromechanics of granular materials
771 with capillary effects. Int J Eng Sci 47:1460–1471. doi: 10.1016/j.ijengsci.2009.10.003
772 25. Golchert DJ, Moreno R, Ghadiri M, et al. (2004) Application of X-ray microtomography
773 to numerical simulations of agglomerate breakage by distinct element method. Adv
774 Powder Technol 15:447–457. doi: 10.1163/1568552041270554
775 26. Fu X, Dutt M, Bentham a. C, et al. (2006) Investigation of particle packing in model
776 pharmaceutical powders using X-ray microtomography and discrete element method.
777 Powder Technol 167:134–140. doi: 10.1016/j.powtec.2006.06.011
778 27. Moreno-Atanasio R, Williams RA, Jia X (2010) Combining X-ray microtomography with
779 computer simulation for analysis of granular and porous materials. Particuology 8:81–99.
780 doi: 10.1016/j.partic.2010.01.001
781 28. Wang Y-H, Leung S-C (2008) A particulate-scale investigation of cemented sand
782 behavior. Can Geotech J 45:29–44. doi: 10.1139/T07-070
783 29. Wang YH, Leung SC (2008) Characterization of Cemented Sand by Experimental and
784 Numerical Investigations. J Geotech Geoenvironmental Eng 134:992–1004.
785 30. Wang J-P, Li X, Yu H-S (2018) A micro – macro investigation of the capillary
786 strengthening effect in wet granular materials . Acta Geotech. doi:
787 doi.org/10.1007/s11440-017-0619-0

788 31. Lame O, Bellet D, Di Michiel M, Bouvard D (2003) In situ microtomography
789 investigation of metal powder compacts during sintering. Nucl Instruments Methods
790 Phys Res Sect B Beam Interact with Mater Atoms 200:287–294. doi: 10.1016/S0168-
791 583X(02)01690-7
792 32. Williams R a., Jia X (2003) Tomographic imaging of particulate systems. Adv Powder
793 Technol 14:1–16. doi: 10.1163/156855203762469867
794 33. Tengattini A, Andò E (2015) Kalisphera: an analytical tool to reproduce the partial
795 volume effect of spheres imaged in 3D. Meas Sci Technol 26:095606. doi:
796 10.1088/0957-0233/26/9/095606
797 34. Aste T, Saadatfar M, Senden T (2005) Geometrical structure of disordered sphere
798 packings. Phys Rev E 71:1–15. doi: 10.1103/PhysRevE.71.061302
799 35. Al-Raoush R (2007) Microstructure characterization of granular materials. Phys A Stat
800 Mech its Appl 377:545–558. doi: 10.1016/j.physa.2006.11.090
801 36. Farber L, Tardos G, Michaels JN (2003) Use of X-ray tomography to study the porosity
802 and morphology of granules. Powder Technol 132:57–63. doi: 10.1016/S0032-
803 5910(03)00043-3
804 37. Aste T, Saadatfar M, Sakellariou a., Senden TJ (2004) Investigating the geometrical
805 structure of disordered sphere packings. Phys A Stat Mech its Appl 339:16–23. doi:
806 10.1016/j.physa.2004.03.034
807 38. Aste T (2005) Variations around disordered close packing. J Phys Condens Matter
808 17:S2361–S2390. doi: 10.1088/0953-8984/17/24/001
809 39. Andò E, Bésuelle P, Hall S a., et al. (2012) Experimental micromechanics: grain-scale
810 observation of sand deformation. Géotechnique Lett 2:107–112. doi:
811 10.1680/geolett.12.00027
812 40. Khaddour G (2005) Multi-scale characterization of the hydro-mechanical behavior of
813 unsaturated sand: water retention and triaxial responses. Université Grenoble Alpes

814 41. Scheel M, Seemann R, Brinkmann M, et al. (2008) Morphological clues to wet granular
815 pile stability. Nat Mater 7:189.
816 42. Khaddour G, Riedel I, Andò E, et al. (2018) Grain-scale characterization of water
817 retention behaviour of sand using X-ray CT. Acta Geotech 13:497–512. doi:
818 10.1007/s11440-018-0628-7
819 43. Wang JP, Lambert P, De Kock T, et al. (2019) Investigation of the effect of specific
820 interfacial area on strength of unsaturated granular materials by X-ray tomography. Acta
821 Geotech. doi: 10.1007/s11440-019-00765-2
822 44. Moscariello M, Cuomo S, Salager S (2018) Capillary collapse of loose pyroclastic
823 unsaturated sands characterized at grain scale. Acta Geotech 13:117–133. doi:
824 10.1007/s11440-017-0603-8
825 45. Newitt DM, Conway-Jones JM (1958) A contribution to the theory and practice of
826 granulation. Trans Inst Chem Eng 36:422.
827 46. Ridler TW, Calvard S (1978) Picture Thresholding Using an Iterative Slection Method.
828 IEEE Trans Syst Man Cybern 8:630–632. doi: 10.1109/TSMC.1978.4310039
829 47. Xie L, Cianciolo RE, Hulette B, et al. (2012) Magnetic resonance histology of age-related
830 nephropathy in the Sprague Dawley rat. Toxicol Pathol 40:764–78. doi:
831 10.1177/0192623312441408
832 48. Peng T, Balijepalli A, Gupta SK, LeBrun T (2007) Algorithms for On-Line Monitoring of
833 Micro Spheres in an Optical Tweezers-Based Assembly Cell. J Comput Inf Sci Eng
834 7:330. doi: 10.1115/1.2795306
835 49. Illingworth J, Kittler J (1987) The Adaptive Hough Transform. IEEE Trans Pattern Anal
836 Mach Intell PAMI-9:690–698. doi: 10.1109/TPAMI.1987.4767964
837 50. Dadda A, Geindreau C, Emeriault F, et al. (2019) Characterization of contact properties in
838 biocemented sand using 3D X-ray micro-tomography. Acta Geotech 14:597–613. doi:
839 10.1007/s11440-018-0744-4

840 51. Lai Z, Chen Q (2019) Reconstructing granular particles from X-ray computed tomography
841 using the TWS machine learning tool and the level set method. Acta Geotech. doi:
842 10.1007/s11440-018-0759-x
843 52. Ding W, Howard AJ, Peri MDM, Cetinkaya C (2007) Rolling resistance moment of
844 microspheres on surfaces: contact measurements. Philos Mag 87:5685–5696. doi:
845 10.1080/14786430701708356
846 53. Santamarina JC (2001) Soil Behavior at the Microscale: Particle Forces. In: Ladd CC (ed)
847 Soil Behav. Soft Gr. Constr. pp 1–32
848 54. Torquato S (2002) Random Heterogeneous Materials: Microstructure and Macroscopic
849 Properties. Springer-Verlag, New York
850 55. Donev A, Torquato S, Stillinger FH (2005) Pair correlation function characteristics of
851 nearly jammed disordered and ordered hard-sphere packings. Phys Rev E - Stat
852 Nonlinear, Soft Matter Phys 71:1–14. doi: 10.1103/PhysRevE.71.011105
853 56. Agnolin I, Roux J-N (2007) Internal states of model isotropic granular packings. I.
854 Assembling process, geometry, and contact networks. Phys Rev E 76:061302. doi:
855 10.1103/PhysRevE.76.061302
856 57. Bruchon J-F, Pereira J-M, Vandamme M, et al. (2013) X-ray microtomography
857 characterisation of the changes in statistical homogeneity of an unsaturated sand during
858 imbibition. Géotechnique Lett 3:84–88. doi: 10.1680/geolett.13.00013
859 58. Gilabert F, Roux J-N, Castellanos a. (2007) Computer simulation of model cohesive
860 powders: Influence of assembling procedure and contact laws on low consolidation
861 states. Phys Rev E 75:011303. doi: 10.1103/PhysRevE.75.011303
862 59. Tang A-M, Cui Y-J, Eslami J, Défossez P (2009) Analysing the form of the confined
863 uniaxial compression curve of various soils. Geoderma 148:282–290. doi:
864 10.1016/j.geoderma.2008.10.012
865 60. Wiebicke M, Andò E, Herle I, Viggiani G (2017) On the metrology of interparticle

contacts in sand from x-ray tomography images. Meas Sci Technol 28:124007.

61. Marmottant A, Salvo L, Martin CL, Mortensen A (2008) Coordination measurements in compacted NaCl irregular powders using X-ray microtomography. J Eur Ceram Soc 28:2441–2449. doi: 10.1016/j.jeurceramsoc.2008.03.041

62. Aste T, Saadatfar M, Senden TJ (2006) Local and global relations between the number of contacts and density in monodisperse sphere packs. J Stat Mech Theory Exp 2006:P07010. doi: 10.1088/1742-5468/2006/07/P07010

63. Al-Raoush RI, Willson CS (2005) Extraction of physically realistic pore network properties from three-dimensional synchrotron X-ray microtomography images of unconsolidated porous media systems. J Hydrol 300:44–64. doi: 10.1016/j.jhydrol.2004.05.005

882 **Figure captions**

883